



Rate constants for the formation of CS by radiative association

R. C. Forrey,¹★ J. F. Babb,² P. C. Stancil³ and B. M. McLaughlin^{2,4}

¹Department of Physics, Penn State University, Berks Campus, Reading, PA 19610-6009, USA

²Institute for Theoretical Atomic, Molecular and Optical Physics (ITAMP), Harvard-Smithsonian Center for Astrophysics, 60 Garden St., Cambridge, MA 02138, USA

³Department of Physics and Astronomy and the Center for Simulation Physics, University of Georgia, Athens, GA 30602, USA

⁴Centre for Theoretical Atomic Molecular and Optical Physics (CTAMOP), School of Mathematics and Physics, Queens University Belfast, Belfast BT7 1NN, UK

Accepted 2018 June 26. Received 2018 June 19; in original form 2017 January 19

ABSTRACT

Rate constants for the formation of carbon monosulfide (CS) by radiative association are calculated using accurate molecular data. The rate constants include both direct and indirect formation processes. The indirect processes (inverse rotational and electronic predissociation) are evaluated for conditions of local thermodynamic equilibrium (LTE) and also in the non-LTE limit of zero radiation temperature and atomic density. Phenomenological rate constants for CS formation in realistic astrophysical environments are expected to lie in-between these limiting cases. An analytic formula is used to fit the rate constants for convenient use in astrophysical models. The impact of the results on various astrophysical environments is briefly discussed.

Key words: astrochemistry – molecular data – molecular processes – ISM: molecules – photodissociation region (PDR) – ISM: supernova remnants.

1 INTRODUCTION

The carbon monosulfide (CS) molecule has been observed in star-forming regions (Walker et al. 1986), protostellar envelopes (Herpin et al. 2012), dense interstellar clouds (Hasegawa et al. 1984; Hayashi et al. 1985; Destree, Snow & Black 2009), carbon-rich stars (Bregman, Goebel & Strecker 1978; Ridgway, Hall & Carbon 1997; Tenenbaum et al. 2010), oxygen-rich stars (Ziurys et al. 2007; Tenenbaum et al. 2010), planetary nebulae (Edwards & Ziurys 2014), and comets (Smith, Stecher & Casswell 1980; Jackson et al. 1982; Canaves et al. 2007).

In interstellar clouds, the CS molecule is one of the most abundant sulfur-bearing compounds, and it is believed (Lucas & Liszt 2002; Neufeld et al. 2015) to be formed primarily by the dissociative recombination (DR) reaction



The branching ratio for process (1) has been measured to be relatively small (19 per cent) with the remaining 81 per cent leading to fracture of the C-S bond (Montaigne et al. 2005).

A spectral emission feature observed at 3.88 micron in the ejecta of supernova SN 1987A within the first year was identified as possibly due to the first overtone transition of CS (Meikle et al. 1989). The chemistry during this period was mainly dust-free, making gas-phase chemical reactions dominant routes to molecule formation and models of molecule formation predicted significant abundances

of CS (Lepp, Dalgarno & McCray 1990). However, subsequent improved chemical models of the mass of CS formed in SN 1987A disagreed significantly with the inferred mass from observations (Liu 1998) and the identification of CS is not considered secure (Cherchneff & Sarangi 2011).

In the absence of hydrogen or dust grains, the CS formation process may be initiated by radiative association (RA) to form SO (Liu 1998)



followed by



or by the direct RA process



where $h\nu$ represents an emitted photon. Molecule formation can also occur through an indirect radiative process, e.g.



where $\text{C} \cdots \text{S}$ represents a metastable state. Semi-classical rate constants for the direct $\text{A}^1\Pi \rightarrow \text{X}^1\Sigma^+$ process were reported by Andreazza, Singh & Sanzovo (1995). The indirect process (5) may include inverse predissociation and generally requires both a dynamical and kinetic formulation for calculating the rate constant. For the iso-electronic SiO molecule, we reported phenomenological RA rate constants (Forrey et al. 2016; Cairnie et al. 2017) for conditions of local thermodynamic equilibrium (LTE) and also for the non-LTE zero-density limit (NLTE-ZDL) which assumes formation

* E-mail: rcf6@psu.edu

occurs through two-body interactions at zero radiation temperature. In the latter case, the tunneling width of a resonant state must be greater than or comparable to the radiative width in order for the indirect process to contribute to the rate. Realistic astrophysical environments containing variable numbers of atoms and photons would be expected to have formation rate constants in-between the LTE and NLTE-ZDL values. In the present work, we report a similar set of rate constants for the formation of CS. The potential energy curves (PECs) and transition dipole moments (TDMs) reported previously (Pattillo et al. 2018) are utilized in the present calculations. The carbon and sulfur atoms are assumed to approach on the $A^1\Pi$, $2^1\Pi$, $3^1\Pi$, $4^1\Pi$, $A^1\Sigma^+$, and $B^1\Sigma^+$ electronic states before forming $X^1\Sigma^+$ bound states.

2 THEORY

As described previously (Forrey 2013, 2015), we utilize a Sturmian representation to form a complete basis set for both the dynamics and kinetics. This allows the density of unbound states for direct and indirect processes to both be incorporated into a single phenomenological cross section. In this formulation, the RA cross-section is defined by

$$\sigma_{\Lambda \rightarrow \Lambda'}(E) = \frac{\pi^2 \hbar^3}{\mu E} P_{\Lambda} \sum_{b,u} g_u (1 + \delta_u) \Gamma_{u \rightarrow b}^{\text{rad}} \delta(E - E_u), \quad (6)$$

where $b \equiv (v_b, j_b)$ and $u \equiv (v_u, j_u)$ designate vibrational and rotational quantum numbers for the respective bound and unbound states of the molecule. Λ and Λ' are projection quantum numbers for the initial and final electronic orbital angular momentum on the internuclear axis, μ is the reduced mass of the C+S system, and E is the translational energy. $\Gamma_{u \rightarrow b}^{\text{rad}}$ is the probability for a radiative transition between the unit-normalized states, and δ_u is a dimensionless parameter which may be computed within a given kinetic model to obtain the density of states with degeneracy $g_u = 2j_u + 1$. The statistical factor

$$P_{\Lambda} = \frac{(2S_{\text{mol}} + 1)(2 - \delta_{0,\Lambda})}{(2L_C + 1)(2S_C + 1)(2L_S + 1)(2S_S + 1)} \quad (7)$$

is determined by L_C , S_C , L_S , and S_S , the electronic orbital and spin angular momenta of the carbon and sulfur atoms, and S_{mol} the total spin of the molecular electronic state.

The spectral properties of the Sturmian representation allow the thermally averaged rate constant

$$k_{\Lambda \rightarrow \Lambda'} = \frac{1}{2\pi Q_T} \int_0^{\infty} E \sigma_{\Lambda \rightarrow \Lambda'}(E) e^{-E/k_B T} dE \quad (8)$$

to be integrated analytically by substituting (6) into (8). The result is

$$k_{\Lambda \rightarrow \Lambda'} = \sum_{b,u} K_u^{\text{eq}} (1 + \delta_u) \Gamma_{u \rightarrow b}^{\text{rad}} \quad (9)$$

where

$$K_u^{\text{eq}} = \frac{(2j_u + 1) P_{\Lambda} \exp(-E_u/k_B T)}{Q_T} \quad (10)$$

is the equilibrium constant for the unbound state, and

$$Q_T = \left(\frac{2\pi \hbar^2}{\mu k_B T} \right)^{-3/2} \quad (11)$$

is the translational partition function for temperature T and Boltzmann's constant k_B . We note that the rate constant (9) includes both direct and indirect formation processes and does not require computation of the cross-section.

The radiative width generally includes spontaneous and stimulated emission and may be written

$$\Gamma_{u \rightarrow b}^{\text{rad}} = \frac{A_{u \rightarrow b}}{1 - e^{-(E_u - E_b)/k_B T_R}} \quad (12)$$

for a pure blackbody radiation field with temperature T_R . The Einstein A-coefficients are given by

$$A_{u_i \rightarrow b_j} = \frac{4}{3c^3} (E_{u_i} - E_{b_j})^3 S_{j_u j_b} |\langle u_i | D | b_j \rangle|^2 \quad (13)$$

and similarly for $A_{u_i \rightarrow u_j}$, where $S_{j,j'}$ are the appropriate line strengths (Cowan 1981; Curtis 2003) or Hönl-London factors (Watson 2008), and c is the speed of light. The electronic dipole moment is defined by

$$D = \begin{cases} \langle \psi_e | p_z | \psi_e' \rangle & \Lambda = \Lambda' \\ \frac{1}{\sqrt{2}} \langle \psi_e | p_x + ip_y | \psi_e' \rangle & \Lambda \neq \Lambda' \end{cases} \quad (14)$$

where (p_x, p_y, p_z) are the components of the dipole operator and ψ_e is the electronic wave function. The TDMs (14) have been calculated previously (Pattillo et al. 2018) for all of the CS electronic states considered in the present work.

The kinetic parameters control the peak heights of the unbound resonances and are determined by the conditions of the gas. For a gas in LTE, the full parameter set is defined by $\delta_{u_i} = 0$. For an NLTE gas, the parameters may be computed from the set of coupled equations (Forrey 2015)

$$1 + \delta_{u_i} = \frac{1 + \tau_{u_i} \sum_j (1 + \delta_{u_j}) \frac{g_{u_j}}{g_{u_i}} e^{-(E_{u_j} - E_{u_i})/k_B T} M_{u_j \rightarrow u_i}}{1 + \tau_{u_i} \left(\sum_j M_{u_i \rightarrow u_j} + \sum_j M_{u_i \rightarrow b_j} \right)} \quad (15)$$

where

$$\tau_{u_i}^{-1} = 2\pi |\langle u_i | V_{\Lambda} | f \rangle|^2 \quad (16)$$

is the elastic scattering width connecting unbound state u_i of the adiabatic potential V_{Λ} to an energy-normalized free eigenstate f with the same energy and angular momentum. The matrix elements $M_{u_i \rightarrow u_j}$ and $M_{u_i \rightarrow b_j}$ include radiative widths (12) and any other type of non-adiabatic coupling. Dissociative transitions, however, are not included in (15), so the formula does not reproduce the LTE limit at high gas densities or when $T = T_R$. For an NLTE-ZDL gas ($T_R = 0$), it is straightforward to show that equation (15) reduces to the usual radiative broadening formula (Forrey 2015)

$$1 + \delta_{u_i} = \frac{1}{1 + \tau_{u_i} \left(\sum_{j < i} A_{u_i \rightarrow u_j} + \sum_j A_{u_i \rightarrow b_j} \right)}. \quad (17)$$

Equation (17) applies to direct processes ($\tau_{u_i} \approx 0$) and to indirect processes ($\tau_{u_i} \gg 0$) such as inverse predissociation via a shape resonance. For a Feshbach resonance ($\tau_{u_i} = \infty$), all bound states of the electronically excited potentials are considered u -states due to their asymptotic energy shift. Therefore, equation (15) reduces to

$$1 + \delta_{u_i} = \frac{\sum_j \Gamma_{u_j \rightarrow u_i}^{\text{pre}}}{\sum_j M_{u_i \rightarrow u_j} + \sum_j M_{u_i \rightarrow b_j}} \quad (18)$$

where

$$\Gamma_{u_j \rightarrow u_i}^{\text{pre}} = 2\pi |\langle u_j | V_{\Lambda' \rightarrow \Lambda} | u_i \rangle|^2 \quad (19)$$

is the predissociation width due to non-adiabatic radial and rotational coupling $V_{\Lambda' \rightarrow \Lambda}$. Equation (18) assumes $\delta_{u_j} = 0$ and that E_{u_j} from V'_{Λ} equals E_{u_i} from V_{Λ} . The denominator in equation (18) includes both predissociation and radiative widths. If there is no

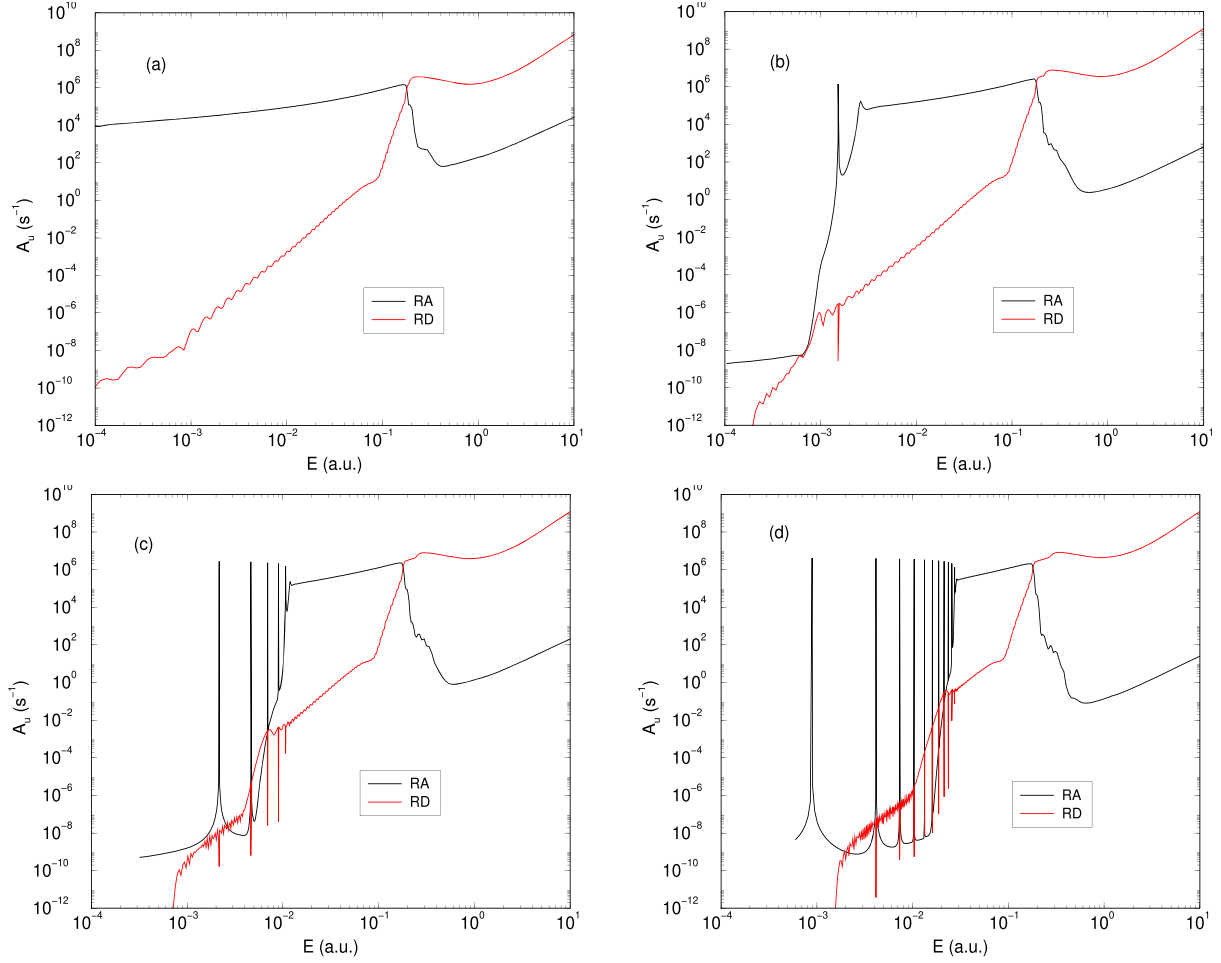


Figure 1. (Colour online) Einstein A-coefficients for initial unbound states in the $A^1\Pi$ potential summed over final states in the $X^1\Sigma^+$ potential. The curves correspond to RA and RD processes for (a) $j_u = 0$, (b) $j_u = 50$, (c) $j_u = 100$, and (d) $j_u = 150$.

asymptotic energy shift between the electronic curves, the radiative broadening formula (17) may be improved using the formula

$$1 + \delta_{u_i} = \frac{1 + \tau_{u_i} \sum_j \Gamma_{u_j \rightarrow u_i}^{pre}}{1 + \tau_{u_i} \left(\sum_{j < i} A_{u_i \rightarrow u_j} + \sum_j A_{u_i \rightarrow b_j} \right)} \quad (20)$$

for an NLTE-ZDL gas. We note that all channel couplings in the above formulation are handled in the framework of time-dependent perturbation theory. Evaluating the density of states from equation (15) ensures that the perturbations are relatively small, even for very narrow resonances.

3 RESULTS

Radiative and tunneling widths were computed using the PECs and TDMs reported previously (Pattillo et al. 2018). Figs 1 and 2 show Einstein A-coefficients as a function of energy for the initial $j_u = 0, 50, 100$, and 150 levels of the $A^1\Pi$ and $A^1\Sigma^+$ potentials as defined by equation (13). The A-coefficients are summed over final states of the $X^1\Sigma^+$ potential. The RA curves sum over the final bound states, and the radiative de-activation (RD) curves sum over the final unbound states. The bound and unbound states are obtained by diagonalizing the adiabatic Hamiltonians in a Sturmian basis set of 500 Laguerre polynomial functions (Forrey 2013). The results show RD is negligible for energies less than ~ 0.1 a.u. but abruptly

dominates RA for higher energies, consistent with previous results for SiO (Cairnie et al. 2017). The direct non-resonant contribution to RA is stronger for the $A^1\Sigma^+$ state than for the $A^1\Pi$ state due to the larger TDM for $A^1\Sigma^+$ (Pattillo et al. 2018). However, the increase in the number of resonances with j_u is greater for $A^1\Pi$ due to the deeper potential well (Pattillo et al. 2018). For example, the number of sharp peaks in Fig. 1 increases from 0 to 1 to 5 to 11 for $j_u = 0, 50, 100$, and 150 . In Fig. 2, the number of sharp peaks changes from 0 to 2 to 3 to 0 for the same values of j_u . The competition between the number of resonances supported by the PEC and the strength of the TDM generally has a strong influence on the temperature dependence of the associated rate constants.

The NLTE-ZDL RA rate constant for $A^1\Pi \rightarrow X^1\Sigma^+$ is shown in Fig. 3. Also shown is the semi-classical result of Andreazza et al. (1995). The semi-classical rate constant does not include resonances and falls off strongly at low temperatures. The NLTE-ZDL rate constant suppresses the contribution from narrow resonances in accordance with equation (17) but includes broad resonances. This provides a more gradual fall-off at low temperature. Both methods appear to reach a maximum around 10,000 K. We present two sets of calculations: the dashed curve includes spontaneous emission using $\Gamma_{u \rightarrow b}^{\text{rad}} = A_{u \rightarrow b}$, and the solid curve includes stimulated emission for a blackbody radiation field using $\Gamma_{u \rightarrow b}^{\text{rad}}$ from equation (12) with $T_R = T$. The figure shows that stimulated RA is not significant for

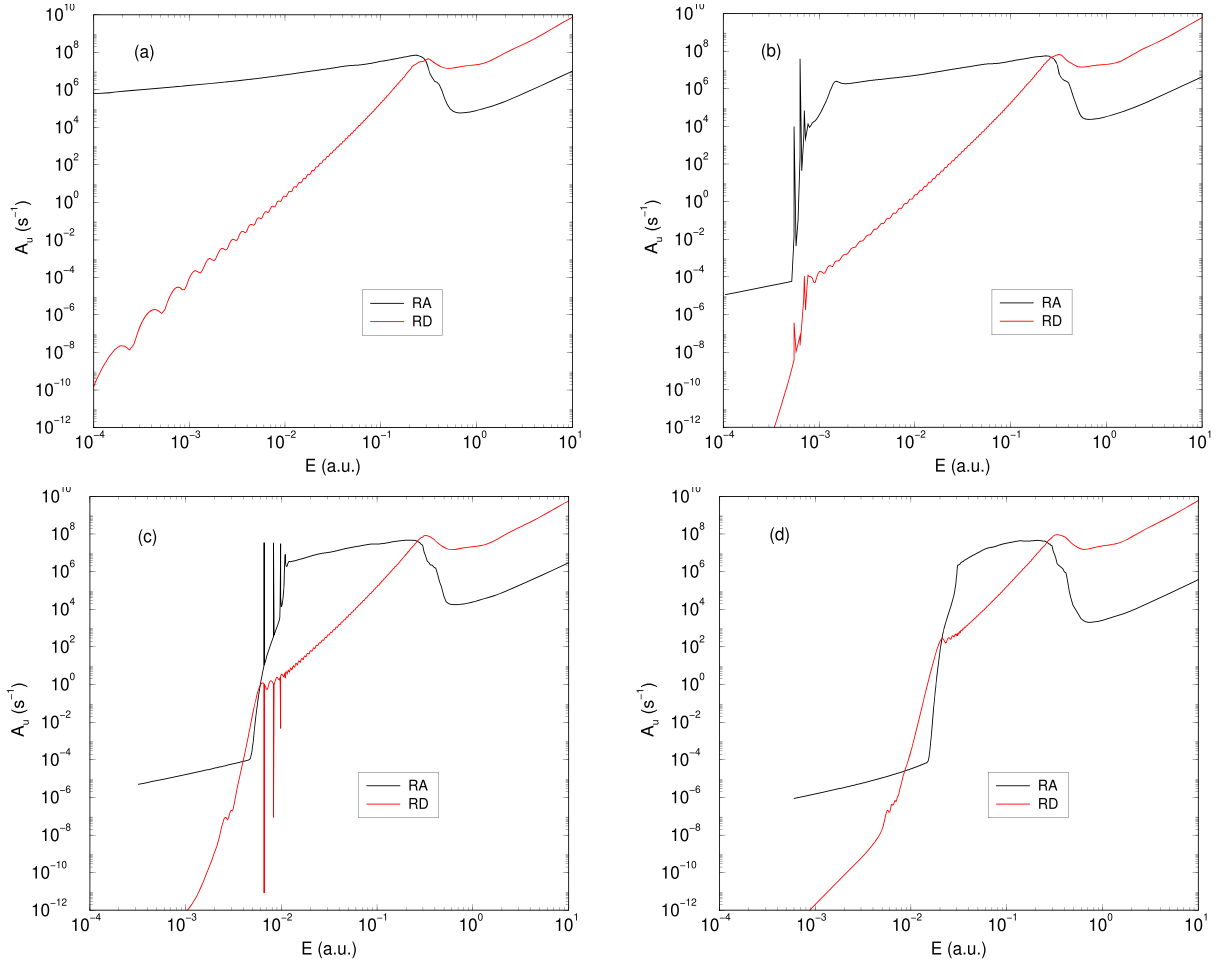


Figure 2. (Colour online) Same as Fig. 1 but for initial unbound states in the $A^1\Sigma^+$ potential. The RA curves in this case are generally larger than the corresponding curves for the $A^1\Pi$ potential, but there are fewer sharp resonance peaks.

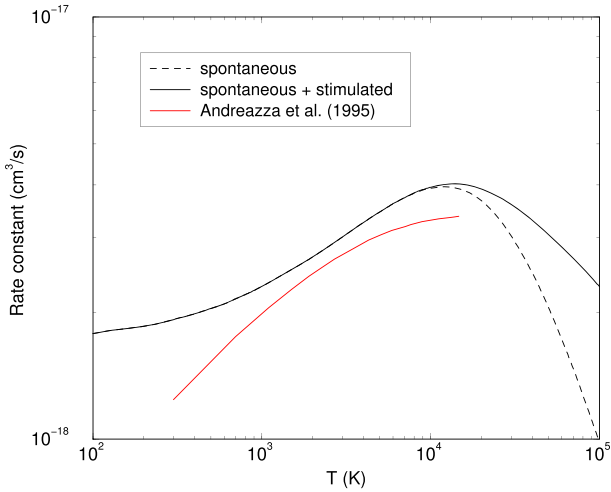


Figure 3. (Colour online) RA rate constants for the $A^1\Pi \rightarrow X^1\Sigma^+$ transition. The dashed black curve corresponds to $\Gamma_{u \rightarrow b}^{\text{rad}} = A_{u \rightarrow b}^{\text{rad}}$. The solid black curve includes spontaneous and stimulated emission for a blackbody radiation field using $\Gamma_{u \rightarrow b}^{\text{rad}}$ from equation (12) with $T_R = T$. Both curves used equation (17) for the kinetic model. The red curve is the semi-classical calculation of Andreazza et al. (1995).

$T < 10,000$ K but provides an enhanced rate constant at higher temperatures.

Rate constants for radiative association to the $X^1\Sigma^+$ state of CS are shown in Fig. 4. The $C(^3P)$ and $S(^3P)$ atoms approach on the $A^1\Pi$, $2^1\Pi$, and $A^1\Sigma^+$ states as shown in the legend. Solid curves correspond to LTE and dashed curves to NLTE-ZDL kinetic models. The LTE and NLTE curves converge in the high temperature region where the importance of the resonant contribution is diminished. The $A^1\Sigma^+$ state provides the largest RA contribution over the entire temperature range due to the strong TDM between the $A^1\Sigma^+$ and $X^1\Sigma^+$ states (Pattillo et al. 2018). The $2^1\Pi$ state yields the second strongest contribution for $T > 10^4$ K. The threshold at lower temperatures is due to a repulsive energy barrier in the $2^1\Pi$ potential. The $A^1\Pi$ rate constant is weakest at high temperature; however, the strong resonant contribution causes the LTE rate constant for this state to approach the $A^1\Sigma^+$ value near 10 K. The difference between the NLTE-ZDL and LTE rate constants is substantial at low temperatures. At 10 K, the LTE rate constants for $A^1\Sigma^+$ and $A^1\Pi$ are larger than their NLTE-ZDL counterparts by a factor of about 13 and 150, respectively. The larger increase in the LTE rate constant for $A^1\Pi$ is due to a deeper potential well which supports more quasibound states.

It is interesting to compare the $A^1\Pi$ rate constants with those reported previously for SiO (Cairnie et al. 2017). The present

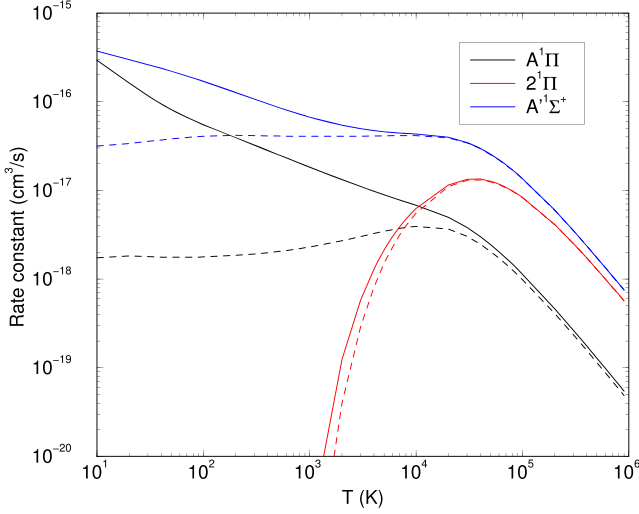


Figure 4. (Colour online) Rate constants for radiative association to the $X^1\Sigma^+$ state of CS. The initial C and S atoms approach on the electronic state given in the legend. Solid curves correspond to LTE and dashed curves to NLTE-ZDL kinetic models. The solid and dashed curves converge in the high-temperature region where the importance of the resonant contribution is diminished.

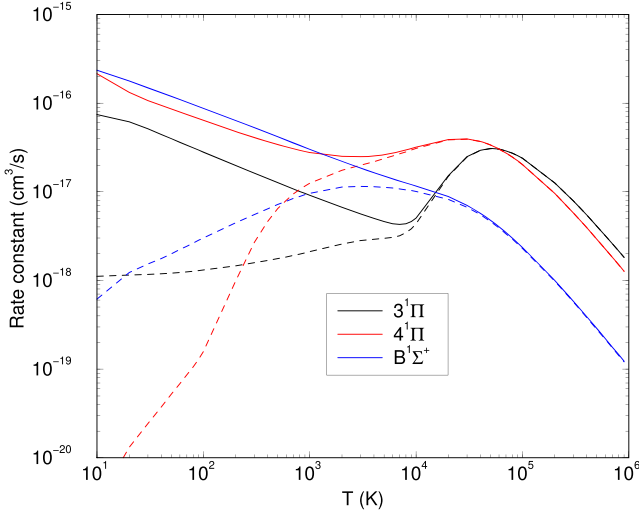


Figure 5. (Colour online) Rate constants for radiative association to the $X^1\Sigma^+$ state of CS. The initial C and S atoms approach on the electronic state given in the legend. Solid curves correspond to LTE and dashed curves to NLTE-ZDL kinetic models. The solid and dashed curves converge in the high-temperature region where the importance of the resonant contribution is diminished.

$A^1\Pi \rightarrow X^1\Sigma^+$ results for CS formation are about an order of magnitude smaller than for SiO formation. This is due to the smaller TDM in the present case. In both cases, the difference between the LTE and NLTE-ZDL models is several orders of magnitude at low temperatures. It should be noted that equation (17) was used for the NLTE-ZDL model in both calculations. There are multiple electronic curves which separate to the $^3P+^3P$ asymptote for both systems, so it is conceivable that the NLTE-ZDL results could be increased if the uncalculated predissociation widths in equation (20) were found to be significant.

Fig. 5 shows rate constants for RA to the $X^1\Sigma^+$ state of CS due to $C(^1D)$ and $S(^1D)$ atoms approaching on the $3^1\Pi$, $4^1\Pi$, and $B^1\Sigma^+$

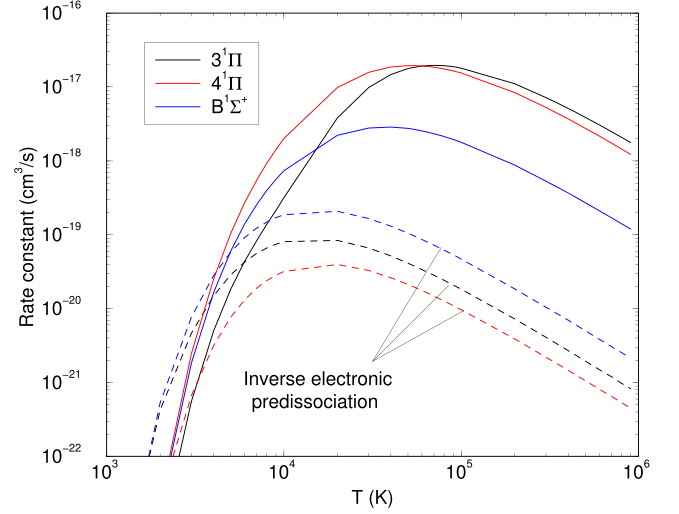


Figure 6. (Colour online) RA and IEP rate constants for the formation of CS in the $X^1\Sigma^+$ state. The solid RA curves are LTE rate constants from Fig. 5 multiplied by the atomic Boltzmann factors for the $C(^1D)+S(^1D)$ asymptote. The dashed IEP curves correspond to a radiationless transition to an intermediate state (denoted by the colour given in the legend) followed by RA to the ground $X^1\Sigma^+$ state.

states. The asymptotic energy for these states is about 2.38 eV larger than the states in Fig. 4 and the atomic part of the statistical factor P_Λ decreases from 81 to 25. The LTE and NLTE behaviour of the rate constants in Fig. 5 is qualitatively similar to those in Fig. 4. The NLTE-ZDL curve for the $4^1\Pi$ state differs from the LTE curve by more than four orders of magnitude at 10 K. This enhanced sensitivity to the kinetic model is due to a very narrow well in the $4^1\Pi$ potential (Pattillo et al. 2018) which supports a large number of quasibound states. The narrow well arises from an avoided crossing with the $3^1\Pi$ potential. The uncalculated predissociation width in equation (20) may be significant in this case, which would increase the population of quasibound $4^1\Pi$ states and the associated NLTE-ZDL rate constant. Figs 4 and 5 show that the rate constants for the $3^1\Pi$, $4^1\Pi$, and $B^1\Sigma^+$ states are comparable to those of the $A^1\Pi$, $2^1\Pi$, and $A^1\Sigma^+$ states.

Molecule formation may also occur through the indirect process of inverse electronic predissociation (IEP). The rate constants for this process are shown in Fig. 6 as dashed curves. The colour indicates the intermediate electronic state given in the legend. For comparison, the LTE rate constants from Fig. 5, multiplied by the atomic Boltzmann factor for these states, are shown as solid curves. Due to approach on a potential with lower asymptotic energy, the thresholds for IEP are shifted slightly to lower temperatures compared to the solid curves. The maximum values of the IEP rate constants are substantially smaller than the corresponding RA curves, especially for the $4^1\Pi$ state where the curves differ by about three orders of magnitude.

The IEP curves in Fig. 6 do not distinguish between LTE and NLTE because differences in the rate constants are assumed to be negligible. Avoided crossings between the $2^1\Pi$ and $3^1\Pi$ potentials and the $3^1\Pi$ and $4^1\Pi$ potentials (Pattillo et al. 2018) suggest there is significant non-adiabatic coupling between these electronic states. These couplings would presumably give rise to large predissociation widths in equations (18). If the predissociation widths are larger than the radiative widths, then the δ_{μ_i} will be close enough to zero that the results of the LTE and NLTE models will be nearly the same.

Table 1. Parameters for the analytic formula (21) used to fit the RA rate constants for approach on the $A^1\Pi$, $2^1\Pi$, and $A'^1\Sigma^+$ states over the temperature range 10 – 10,000 K.

Fitting parameter	$A'^1\Sigma^+ \rightarrow X^1\Sigma^+$		$A^1\Pi \rightarrow X^1\Sigma^+$		$2^1\Pi \rightarrow X^1\Sigma^+$	
	LTE	NLTE-ZDL	LTE	NLTE-ZDL	LTE	NLTE-ZDL
a	0.955744	0.091797	0.153069	0.020087	0	0
b	0.400933	0.328056	0.787454	-0.063569	0	0
c_1	43.21563	4.636323	7.554797	2.141587	0.924243	1.318363
c_2	24.77612	3.189929	8.042786	1.862235	1.618295	1.029097
c_3	34.66025	15.11480	7.541511	1.649521	2.909239	3.998898
d_1	8684.089	483.6360	156.9699	3710.579	17583.64	10344.45
d_2	4842.372	50.86205	2213.844	12269.08	8942.581	13859.56
d_3	8874.313	4087.619	2403.755	12061.18	11767.33	33440.38
e_1	0.638449	0.401756	0.611547	0.563279	0.170245	0.522451
e_2	0.589669	0.442853	0.679699	0.538354	0.384268	0.186535
e_3	0.641479	0.431464	0.683191	0.572388	0.484086	0.376133

Table 2. Parameters for the analytic formula (21) used to fit the RA rate constants for approach on the $3^1\Pi$, $4^1\Pi$, and $B^1\Sigma^+$ states over the temperature range 10 – 10,000 K.

Fitting parameter	$B^1\Sigma^+ \rightarrow X^1\Sigma^+$		$3^1\Pi \rightarrow X^1\Sigma^+$		$4^1\Pi \rightarrow X^1\Sigma^+$	
	LTE	NLTE-ZDL	LTE	NLTE-ZDL	LTE	NLTE-ZDL
a	0.305523	0.001298	0.141944	0.017278	0.374976	0.001069
b	0.581708	0.392968	0.490422	-0.179136	0.395249	-0.698282
c_1	6.095590	2.281119	2.001352	1.683982	3.412438	2.963747
c_2	13.92909	4.609992	2.858530	1.904914	2.071203	2.642933
c_3	10.52673	1.344122	2.322341	2.044345	2.596159	2.175024
d_1	67.29391	59.68620	4014.434	36269.18	13300.08	12116.77
d_2	4530.670	1442.135	9981.163	18405.18	10503.79	5816.140
d_3	956.0077	248.3015	35778.87	18688.71	4017.053	839.5973
e_1	0.601948	0.966942	0.627538	0.126588	0.290190	0.283340
e_2	0.641292	0.444759	1.113974	0.931110	0.711764	0.300441
e_3	0.703725	0.456567	0.145105	0.969716	0.275912	0.296462

We also note that the thresholds for the RA curves in Fig. 6 occur at relatively high energies where the influence of quasibound states is expected to be reduced. Therefore, the differences between LTE and NLTE are expected to be less important for these states.

It would be interesting to calculate the non-adiabatic predissociation widths for all of the states to see whether they have a significant influence on the NLTE rate constants. This will be considered in our future work on this system.

4 ASTROPHYSICAL APPLICATIONS

To allow for convenient use of the current results in astrophysical models, we adopt the analytic fitting formula

$$k_r = \left[a(400/T)^b + \sum_{i=1}^3 c_i T^{-e_i} \exp(-d_i/T) \right] \times 10^{-16} \text{ cm}^3/\text{s} \quad (21)$$

for both LTE and NLTE-ZDL rate constants. Fixing the temperature exponent $e_i = 1.5$ mimics the Q_T contribution in equation (10) and has yielded good fits in previous work (Novotný et al. 2013; Vissapragada et al. 2016; Cairnie et al. 2017). In the present work, we find better results by allowing these exponents to be unconstrained. The fitting parameters for the $A^1\Pi$, $2^1\Pi$, and $A'^1\Sigma^+$ states are given in Table 1. Additional parameters for the $3^1\Pi$, $4^1\Pi$, and $B^1\Sigma^+$ states are given in Table 2. The LTE results for IEP are given in Table 3. The analytic formula (21) provides a fit to the rate constants to better than 10 percent over the temperature range 10 – 10,000 K. The formula performs poorly outside this temperature range. The sup-

Table 3. Parameters for the analytic formula (21) used to fit the IEP rate constants for the intermediate $3^1\Pi$, $4^1\Pi$, and $B^1\Sigma^+$ states over the temperature range 10 – 10,000 K. Here, the LTE and NLTE rate constants are assumed to be identical (see text).

Fitting parameter	$B^1\Sigma^+ \rightarrow X^1\Sigma^+$	$3^1\Pi \rightarrow X^1\Sigma^+$	$4^1\Pi \rightarrow X^1\Sigma^+$
a	0	0	0
b	0	0	0
c_1	1.408350	6.571382	22.92551
c_2	22.48106	4.194277	33.07684
c_3	25.51743	12.33085	27.11157
d_1	17204.09	16566.49	20861.47
d_2	17530.32	15117.88	22629.95
d_3	17544.67	17529.16	22228.48
e_1	0.900671	0.977559	1.087009
e_2	0.929925	0.896032	1.152190
e_3	0.930996	0.944455	1.136984

plementary material provides plots which compares equation (21) with exact numerical results.

As a test of the current RA rate constants, we consider the Leiden photodissociation region (PDR) benchmark models (Röllig et al. 2017) which are available as part of the test suite for the astrophysical simulation code Cloudy (Ferland et al. 2017). All of the eight models assume constant gas densities (10^3 or $10^{5.5} \text{ cm}^{-3}$), an incident scaled UV radiation field (10 or 10^5 times the standard interstellar radiation field (ISRF)), and the standard set of UMIST

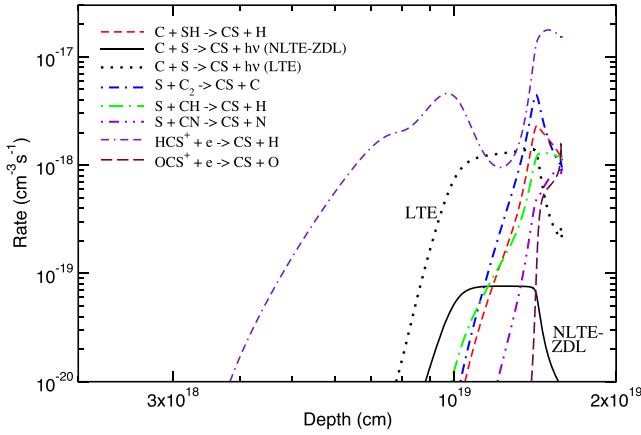


Figure 7. (Colour online) CS formation rates as a function of cloud depth for the dominant processes for the Leiden PDR benchmark model v2 as obtained with Cloudy c17 for a density of 10^3 cm^{-3} and 10^5 times the ISRF. The CS RA formation rate for both the NLTE-ZDL and LTE limits are shown.

chemical rate coefficients (McElroy et al. 2013). Four models assume a constant gas temperature of 50 K, while the other four self-consistently solve for the gas and grain temperature as a function of depth into the cloud (see Ferland et al. 2017, for details). In most models, the formation of CS is dominated by HCS^+ DR (process 1). However, in some cases, the reactive scattering process



becomes the primary formation mechanism deep into the cloud, where the electron fraction is small. Unlike previous modelling, which considered only the NLTE-ZDL semi-classical CS RA rate constant from Andreazza et al. (1995) for the $\text{A}^1\Pi\text{-X}^1\Sigma^+$ transition (e.g. McElroy et al. 2013), we also include the CS RA rate for the $\text{A}^1\Sigma\text{-X}^1\Sigma^+$ which Fig. 4 shows to be typically an order of magnitude larger than the former for both the NLTE-ZDL and LTE rates.

As an illustration, Fig. 7 gives the dominant CS formation rates as a function of depth into the PDR. HCS^+ dominates at all depths, but CS RA is the second most important process near 10^{19} cm when the NLTE-ZDL rate constant is adopted. Conversely, if the CS LTE RA rate constant is applied, it becomes the dominant formation mechanism at this same depth.

The ejecta of a Type II supernova (SN) is deficient in H as most of the hydrogen was lost in outflows during the AGB phase of the progenitor. Further, while the ejecta is somewhat stratified, there is significant mixing of C, O, Si, and S. As a consequence, Fig. 7 and the arguments in Liu (1998) suggest that radiative association of C and S may play an important role in CS formation since HCS^+ DR, and the other reactions involving H in Fig. 7, would be absent from the SN chemical network.

5 CONCLUSIONS

We have calculated rate constants for the formation of CS by radiative association using accurate molecular data. The rate constants are evaluated for kinetic conditions of LTE and NLTE-ZDL. Rate constants for realistic astrophysical environments generally fall in-between these two limiting cases. For dark low-density environments, the NLTE-ZDL rate constant should be used. As the density of atoms and/or photons increases, the steady-state formation rate

constant increases towards the LTE value. The difference between these two limits is large at low temperatures, particularly for the $\text{A}^1\Pi$ contribution. This is due to a deep potential well that supports many quasi-bound states. The relatively shallow $\text{A}^1\Sigma^+$ potential supports fewer quasi-bound states, so the difference between the LTE and NLTE-ZDL values for this state is substantially smaller than for the $\text{A}^1\Pi$ state. The rate constant, however, is largest for the $\text{A}^1\Sigma^+$ state due to the strong TDM for the $\text{A}^1\Sigma^+ \rightarrow \text{X}^1\Sigma^+$ transition. Rate constants for molecule formation in the $\text{A}^1\Pi$ and $\text{A}^1\Sigma^+$ potentials were found to be negligible and are not reported. Incorporation of the new CS radiative association rate constants, which are significantly larger than values found in the literature, may enhance the total CS abundance in interstellar environments, particularly those deficient in hydrogen and grains.

ACKNOWLEDGEMENTS

RCF acknowledges support from NSF Grant No. PHY-1503615. PCS acknowledges support from NASA grant NNX16AF09G. BMMcL acknowledges support from the ITAMP visitor's program, Queen's University Belfast for the award of a Visiting Research Fellowship (VRF), and the hospitality of the University of Georgia during recent research visits. ITAMP is supported in part by a grant from the NSF to the Smithsonian Astrophysical Observatory and Harvard University. The computational work was performed on local clusters, the National Energy Research Scientific Computing Centre in Berkeley, CA, USA and at The High Performance Computing Centre Stuttgart (HLRS) of the University of Stuttgart, Stuttgart, Germany. Grants of computing time at NERSC and HLRS are gratefully acknowledged.

REFERENCES

- Andreazza C. M., Singh P. D., Sanzovo G. C., 1995, *ApJ*, 451, 889
- Bregman J. D., Goebel J. H., Strecker D. W., 1978, *ApJ*, 223, L45
- Cairnie M., Forrey R. C., Babb J. F., Stancil P. C., McLaughlin B. M., 2017, *MNRAS*, 471, 2481
- Canaves M., de Almeida A., Boice D., Sanzovo G., 2007, *AdSpR*, 39, 451
- Cherchneff I., Sarangi A., 2011, in Cernicharo J., Bachiller R., eds, *Proc. IAU Symp. 280, The Molecular Universe*. Cambridge Univ. Press, Cambridge
- Cowan R. D., 1981, *The Theory of Atomic Structure and Spectra*. University of California Press, Berkeley, California, USA
- Curtis L. J., 2003, *Atomic Structure and Lifetimes: A conceptual Approach*. Cambridge Univ. Press, Cambridge, UK
- Destree J. D., Snow T. P., Black J. H., 2009, *ApJ*, 693, 804
- Edwards J. L., Ziurys L. M., 2014, *ApJ*, 794, L27
- Ferland G. J. et al., 2017, *Rev. Mex. Astron. Astrofis.*, 53, 385
- Forrey R. C., 2013, *Phys. Rev. A*, 88, 052709
- Forrey R. C., 2015, *J. Chem. Phys.*, 143, 024101
- Forrey R. C., Babb J. F., Stancil P. C., McLaughlin B. M., 2016, *J. Phys. B*, 49, 18
- Hasegawa T. et al., 1984, *ApJ*, 283, 117
- Hayashi M., Omodaka T., Hasegawa T., Suzuki S., 1985, *ApJ*, 288, 170
- Herpin F. et al., 2012, *A&A*, 542, A76
- Jackson M. W., Halpern J. B., Feldman P. D., Rahe J., 1982, *A&A*, 107, 385
- Lepp S., Dalgarno A., McCray R., 1990, *ApJ*, 358, 262
- Liu W., 1998, *ApJ*, 496, 967
- Lucas R., Liszt H. S., 1984, *A&A*, 384, 1054
- McElroy D., Walsh C., Markwick A. J., Cordiner M. A., Smith K., Millar T. J., 2013, *A&A*, 550, A36
- Meikle W. P. S., Allen D. A., Spyromilio J., Varani G.-F., 1989, *MNRAS*, 238, 193
- Montaigne H. et al., 2005, *ApJ*, 631, 653
- Neufeld D. A. et al., 2015, *A&A*, 577, A49

- Novotný O. et al., 2013, *ApJ*, 777, 54
 Pattillo R. J., Cieszewski R., Stancil P. C., Forrey R. C., Babb J. F., McCann J. F., McLaughlin B. M., 2018, *ApJ*, 858, 10
 Ridgway S. T., Hall D. N. B., Carbon D. F., 1997, *BAAS*, 9, 636
 Rölling M. et al., 2007, *A&A*, 467, 187
 Smith A. M., Stecher T. P., Casswell L., 1980, *ApJ*, 242, 402
 Tenenbaum E. D., Dodd J. L., Milam S. N., Woolf N. J., Ziurys L. M., 2010, *ApJS*, 190, 348
 Vissapragada S., Buzard C. F., Miller K. A., O'Connor A. P., de Ruelle N., Urbain X., Savin D. W., 2016, *ApJ*, 832, 31
 Walker C. K., Lada C. J., Young E. T., Maloney P. R., Wilking B. A., 1986, *ApJ*, 309, L47
 Watson J. G. K., 2008, *JMoSp*, 253, 5
 Ziurys L. M., Milam S. N., Apponi A. J., Woolf N. J., 2007, *Nature*, 447, 1094

SUPPORTING INFORMATION

Supplementary data are available at *MNRAS* online.

Please note: Oxford University Press is not responsible for the content or functionality of any supporting materials supplied by the authors. Any queries (other than missing material) should be directed to the corresponding author for the article.

Figure S1 IEP rate constants using parameters from Table 3.

Figure S2 RA rate constants using parameters from Table 1.

Figure S3 RA rate constants using parameters from Table 2.

Figure S4 RA rate constants using parameters from Table 1 and Table 2.

This paper has been typeset from a \TeX/L\AA\TeX file prepared by the author.